Fuel 310 (2022) 122302

Contents lists available at ScienceDirect

Fuel

journal homepage: www.elsevier.com/locate/fuel

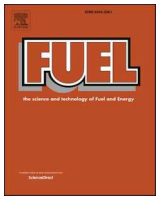

Full Length Article

The significance of intraparticle and interparticle diffusion during CO_2 gasification of biomass char in a packed bed

Aekjuthon Phounglamcheik [a,*], Markus Bäckebo [a], Ryan Robinson [b], Kentaro Umeki [a]

[a] Division of Energy Science, Luleå University of Technology, SE-971 87 Luleå, Sweden
[b] Global Technology, Höganäs AB, Höganäs, Sweden

ARTICLE INFO

Keywords:
Biomass char
Packed bed
CO_2 gasification rate
Intraparticle diffusion
Interparticle diffusion
Particle size distribution

ABSTRACT

This study investigates the influences of intraparticle and interparticle diffusions on the reaction rates of char gasification in a packed bed without forced convective flows. The main objective is to elucidate how the dominant scales of mass diffusion resistance change based on particle size distributions (PSD). CO_2 gasification rates were measured by thermogravimetric analyses (TGA) of spruce char produced from pilot-scale reactors. Experimental setups using two TGA devices highlighted the effects on different rate-limiting steps. Effects of intraparticle diffusion were investigated with a single layer of monodispersed particles between 75 μm and 6.3 mm using a commercial TGA. Effects of interparticle diffusion were investigated with a packed bed of monodispersed and polydispersed particles using a macro-TG. At the particle scale, gasification rate decreased with the increase of particle size when the reaction was controlled by intraparticle diffusion. This effect can be described by the effectiveness factor with Thiele modulus. At the bed scale, void fraction and tortuosity of the packed bed are influential parameters on diffusivity of CO_2 through the bed channels. Due to its non-sphericity of the char particles, the bed of relatively large particles had high void fraction and the presence of smaller particles were essential to lower the bed void size. Consequently, smaller size fraction in the PSD had a major impact on the diffusion resistance at bed scale. It means that the diffusion resistances at particle and bed scales are sensitive to different size fractions in the PSD. It allows one to tweak the overall reaction rates in packed beds by manipulating the PSD if the dominant mass transport mechanism is diffusion.

1. Introduction

In recent years, many research activities have dedicated efforts to reduce greenhouse gas emissions from iron and steelmaking processes. The steel industry contributes 7% of the global total CO_2 emission, which is around 2.8 billion tons annually [1]. Sustainable steelmaking plants shall diminish the use of fossil-based raw materials. Our previous review [2] summarized the state-of-the-art to utilize bio-reducers in various steelmaking routes, for example, blast furnace/basic oxygen furnace (BF-BOF) route and direct reduction iron/electric arc furnace (DRI-EAF) route. Biomass char has great potential to replace fossil coal in steelmaking plants [2–4]. The highest potential of biomass char usage is in the BF-BOF route [2], both as biocoke [5] and injection fuel [6]. A recent study reported the successful replacement of one-third of carburization media in an EAF process by biomass char [7]. Among the DRI processes, biomass char can replace fossil-based carbon as a reducing agent in some processes, such as the Höganäs process. Here, the reduction of iron progresses in a sagger without convective flows. The sagger contains a packed bed of solid reducing agent and iron ore without intermixing.

In order to avoid major process modifications, various properties of biomass char should be equivalent to those of fossil-based reducing agents. Our previous studies [8,9] showed that elemental composition and heating value of biomass char could reach the same level as fossil coal if pyrolyzed at temperatures above 500 °C, with the exception of gasification reactivity. In the carbon-based DRI process, the reduction of iron ore occurs with a series of chemical reactions.

$$C(s) + CO_2(g) \rightarrow 2CO(g) \quad (R1)$$

$$Fe_3O_4(s) + CO(g) \rightarrow 3FeO(s) + CO_2(g) \quad (R2)$$

$$3FeO(s) + 3CO(g) \rightarrow 3Fe(s) + 3CO_2(g) \quad (R3)$$

The rate of char gasification (Reaction (1)), known as Boudouard

* Corresponding author.
E-mail address: aekjuthon.phounglamcheik@ltu.se (A. Phounglamcheik).

https://doi.org/10.1016/j.fuel.2021.122302
Received 10 May 2021; Received in revised form 2 September 2021; Accepted 14 October 2021
Available online 23 October 2021

reaction, is a critical step as it determines the availability of reducing gas, i.e., CO. This fact also applies to other steelmaking routes. The different physical and chemical structures between fossil coals and biomass char result in different gasification reactivity. It has been widely reported that the reactivity of biomass chars is generally higher than those of fossil coals [10–12]. Zuo et al. [13] reported that biomass char reacted four time faster than anthracite coal in CO_2 gasification at 850–1000 °C. Case in point, the Höganäs process currently utilizes fossil-based reducing agents that maintain an even rate of gasification over a relatively long residence time in the furnace, i.e., 2–3 days. Consequently, replacing these fossil-based reducing agents with more reactive biomass char would yield incomplete iron conversion in the existing process. Hence, the gasification rate of biomass char must be controlled to an acceptable range in order to increase implementation of bio-reducers in this process. In addition, the Höganäs process converts iron reduction in a saggar, where diffusion dominates overall mass transfer rate without forced convective flows. This reactor configuration is different from typical metallurgical and thermochemical reactors, thus limited studies appear in the literature.

Char gasification involves three phenomena that are possible rate-limiting steps: chemical reaction, intraparticle diffusion, and interparticle diffusion. In the most industrially relevant conditions, the gasification rate of biomass char is affected by intraparticle diffusion, also referred to as pore diffusion [14]. The diffusion rate of CO_2 through the pore inside char particles plays a significant role in the overall reaction rate. In this case, particle size, density, and pore structure affect the apparent reactivity of char gasification. The literature agrees that apparent char reactivity decreases as the particle size increases [15–18]. For instance, Gómez-Barea et al. [15] measured char gasification rates under CO_2 at 800 °C, and the result showed that effectiveness factor decreased from 0.9 to 0.55 when particle size increased from 0.9 to 2.1 mm. This observation is in line with the Thiele modulus [19], i.e., the ratio of surface reaction rate to the rate of diffusion, which implies that the larger the particles, the higher the diffusional resistance. In general, the effect of intraparticle diffusion is negligible below a certain threshold of particle size. Guizani et al. [16] reported that intraparticle diffusion did not affect the apparent reactivity of the particles smaller than 40 μm. Nevertheless, the threshold may be different for char samples with different density and pore structure, and it varies with gasification conditions.

In a packed bed of bio-coal without forced convective flow, such as saggar crucibles, external and interparticle diffusions affect the apparent reaction rate along with intraparticle diffusion. Unlike the other two rate-limiting steps, few studies appear in the literature. External diffusion is caused by CO_2 diffusion in the stagnant gas region between the top of the packed bed and the bed surface, while interparticle diffusion is CO_2 diffusion through the channels (voids) between the particles in the packed bed. In some cases, external diffusion may also influence apparent reactivity [20]. Meanwhile, Zhang et al. reported [21] that interparticle diffusion had more significant effects than external diffusion in gasification of lignite char. They found that the effect of interparticle diffusion increased exponentially with bed height. This result agrees with the study of waste biomass gasification reported by Ollero et al. [22]. Particle size distribution should be an important parameter for the apparent reactivity of packed beds with a given bed volume because of its effects on physical properties, such as bed void fraction, tortuosity, and channel size. Zhang et al. [23] showed that the bed void fraction of solid particles increased with the decrease of particle size. They also reported that particle shape influences the void fraction. These observations imply that the effect of interparticle diffusion should be more significant for larger particles. However, interparticle channels among small particles should be narrower than those among large particles, and hence, more significant interparticle diffusion effects. Furthermore, the uniformity in particle size distribution (PSD) affects the permeability in packed beds [24–27], and it should also influence the effective mass diffusivity. This means that monodispersed, bimodal, and polydispersed particles differ interparticle diffusion in a packed bed. In addition, interparticle and intraparticle diffusions simultaneously plays roles in a bed due to various particle sizes. However, to the best of our knowledge, no previous work investigated particle size or PSD effects on char gasification in a packed bed under the absence of convective flow.

To understand and predict the heterogeneous reactions in packed beds, such as char gasification, holistic studies across all the relevant scales are necessary. This study aims to identify the individual effects of particle-scale diffusion and bed-scale diffusion, as well as their interactions. Specifically, it intends to elucidate the effect of particle size and PSD at bed scale in detail. Measurement was carried out in two different sizes of thermogravimetric analysis (TGA) devices suitable for particle-scale and bed-scale investigation. Gasification rates of monodispersed, bimodal, and polydispersed particles have been measured. The intrinsic rate constant has been determined based on the *n*th-order kinetic model, while the effects of intraparticle and interparticle diffusions have been determined by using the effectiveness factor approach. Terminologies were defined and used to explain the phenomena at different scales, as summarized in Table 1.

2. Materials and methods

2.1. Sample preparation

Biomass char used in this study was obtained from a 500 $kW_{thermal}$ two-step pyrolysis process operated by Cortus AB, Sweden [28]. In the first step, the biomass char was produced from dried spruce chips (including bark), approximately 20–50 mm size, in a rotary kiln reactor at the temperature of 350 °C with the residence time of ca. 1 h. Then, secondary pyrolysis was carried out in a retort (moving bed) at a temperature of 1100 °C with a residence time of 20–30 min. After pyrolysis, the biomass char was extruded into cylindrical pellets, approximately 12 mm diameter and 50 mm length, in order to increase the particle density. Thereafter, the char pellets were crushed using a disintergretor mill, BAC 15, to achieve the relevant particle size distribution. Prior to analysis and experiment, the biomass char was dried in an oven at 40 °C for 12 h to remove raw moisture following the European Biochar Certificate guideline [29]. The char sample was divided into smaller portions by using a rotary divider, Retsch PT100.

Particle size distribution was measured by using the sieving method according to ASTM C 136–01. A stack of stainless sieves with mesh aperture widths of 0.18, 0.212, 0.315, 0.4, 0.5, 0.63, 0.8, 1.0, 2.0, 3.15, 4.0, 5.0, 6.3, and 7.1 mm was used with a mechanical sieve shaker, Retsch AS200. Around 70 g of sample was used in the measurement. The microscopic images of the sieved particles, measured using VisiScope® BL254 T1, are provided in Figure S1 in the supplementary material. The images show equivalent sizes between the actual sizes and the sieve sizes of particles. Fig. 1 displays the PSD of the as-received sample, together with all the PSDs used in this study (summarized in Table 3).

In order to study the effect of particle size on reaction rates, seven narrow size fractions, hereafter called monodispersed particle samples, have been selected as shown in Table 2. These size fractions cover the range of particle size distribution of the biomass char sample. The terms d_{min}, d_{max}, and d_{mid} refer to minimum, maximum, and mid-range

Table 1
Summary of important terminologies.

Terms	Void/pore	Rate constant	Diffusion	Effectiveness factor
Global	–	–	Overall	Overall
Bed scale	Void fraction	Bed	Interparticle	Bed
Particle scale	Porosity	Particle	Intraparticle	Intraparticle
Reactive surface	–	Intrinsic	–	–

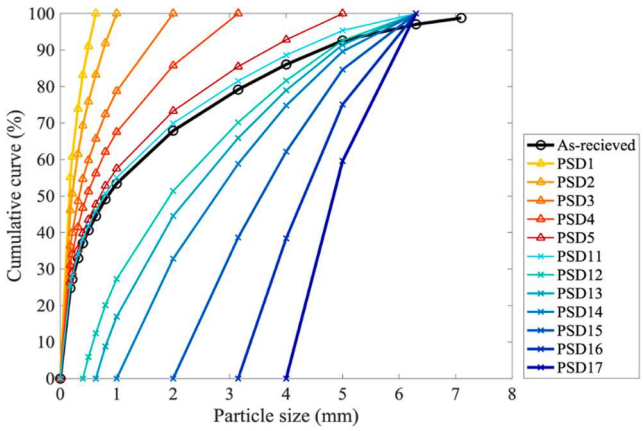

Fig. 1. Cumulative curves of the samples.

Table 2
Size characteristics of monodispersed particle samples.

Sample	d_{min} (μm)	d_{max} (μm)	d_{mid} (μm)
d_{p1}	–	75	–
d_{p2}	180	212	196
d_{p3}	315	400	358
d_{p4}	500	630	565
d_{p5}	800	1000	900
d_{p6}	2000	3150	2575
d_{p7}	4000	6300	5150

particle sizes.

In addition to the monodispersed particle samples, samples with wide ranges of the particle size distribution, hereafter called polydispersed samples, were prepared within the particle range of 180 and 6300 μm, as shown in Fig. 1. The samples with the labels PSD1 to PSD5 were prepared by decreasing the maximum diameter of the PSD in comparison with as-received PSD. In contrast, the samples PSD11 to PSD17 were prepared by increasing the minimum diameter. Table 3 shows the size characteristics of the varied PSD samples. The term d_{50} refers to mass-based median particle size, i.e., the screen sizes being passed 50% by mass of the particles. Meanwhile, d_{10}, d_{30}, and d_{60} are the screen sizes being passed 10, 30, and 60% by the mass of the particles. The term μ and σ represent the mean and standard deviation of the log-normal distribution of the PSD. The small value of σ refers to the narrow range of particle size, while large σ refers to a wide range of particle size.

2.2. Sample characterization

The density of the biomass char was measured by three different definitions, that is, bulk density, envelope density, and skeleton density. The bulk density was measured according to analogue VDLUFA-Method A 13.2.1 [30]. For the as-received sample, the sample was placed into a 500 mL graduated cylinder with 5 mL of increment. The volume and mass were measured after compressing the cylinder by tapping the bottom of the cylinder ten times. The bulk density of the monodispersed and PSD samples was measured directly with the ceramic crucible, 6.5 mL of bed volume, prior to the gasification experiment by using the same procedure. The measurement was repeated three times. Bulk density was calculated by

$$\rho_{bulk} = \frac{m_{char}}{V_{b,char}} \tag{1}$$

where m_{char} and $V_{b,char}$ are mass and bed volume of biomass char, respectively.

In the measurement of envelope density, 15 mL of Al_2O_3 (particle size distribution is provided in the supplementary material, Table S1) was filled into a graduated cylinder (25:0.5 mL), and the initial mass was measured. Then, 3–5 mL of the sample was added into the cylinder, and the sample was immersed into Al_2O_3 by manual shaking. The measurement was repeated three times. The mass and volume were recorded. Finally, envelope density was calculated by

$$\rho_{envelope} = \frac{m_{char}}{V_{p,char}} = \frac{m_{char+Al_2O_3} - m_{Al_2O_3}}{V_{b,char+Al_2O_3} - V_{b,Al_2O_3}} \tag{2}$$

where $V_{p,char}$ is particle volume including internal pores of biomass char.

Skeleton density, or true density, was measured by using Micromeritics AccuPyc II 1340 gas displacement pycnometer with He as the gas medium. Prior to this measurement, the sample was dried further at 105 °C to remove all the moisture in the particles. During the measurement, He gas filled in both bed voids and open pores of particles, making it possible to estimate the volume of solid materials. The skeleton density was calculated based on the principle of volume displacement

$$\rho_{skeleton} = \frac{m_{char}}{V_{s,char}} \tag{3}$$

where $V_{s,char}$ is solid volume including closed pores of biomass char.

Particle porosity, $\varepsilon_{particle}$, and bed void fraction, ε_{bed}, can be calculated by

$$\varepsilon_{particle} = \frac{V_{p,char}}{V_{s,char}} = 1 - \frac{\rho_{envelope}}{\rho_{skeleton}} \tag{4}$$

$$\varepsilon_{bed} = \frac{V_{b,char}}{V_{p,char}} = 1 - \frac{\rho_{bulk}}{\rho_{envelope}} \tag{5}$$

Fig. 2 depicts void fractions of the monodispersed and polydispersed samples. The error bars represent standard deviations of void fractions calculated based on the error propagation from the standard deviations

Table 3
Size characteristics of varied polydispersed samples.

Sample	d_{min} (μm)	d_{max} (μm)	d_{10} (μm)	d_{30} (μm)	d_{50} (μm)	d_{60} (μm)	μ (-)	σ (-)
PSD1	<180	630	32	100	160	205	−1.77	0.80
PSD2	<180	1000	39	115	210	300	−1.57	1.15
PSD3	<180	2000	50	150	320	500	−1.11	1.39
PSD4	<180	3150	58	175	450	740	−0.80	1.42
PSD5	<180	5000	68	230	670	1160	−0.48	1.71
PSD11	<180	6300	72	250	850	1400	−0.40	1.72
PSD12	400	6300	600	1100	1940	2500	0.59	0.89
PSD13	630	6300	840	1480	2300	2800	0.79	0.74
PSD14	1000	6300	1300	1900	2770	3200	1.04	0.47
PSD15	3150	6300	2300	2900	3560	3900	1.29	0.32
PSD16	4000	6300	3400	3800	4300	4600	1.45	0.21
PSD17	5000	6300	4200	4500	4840	5000	1.60	0.03

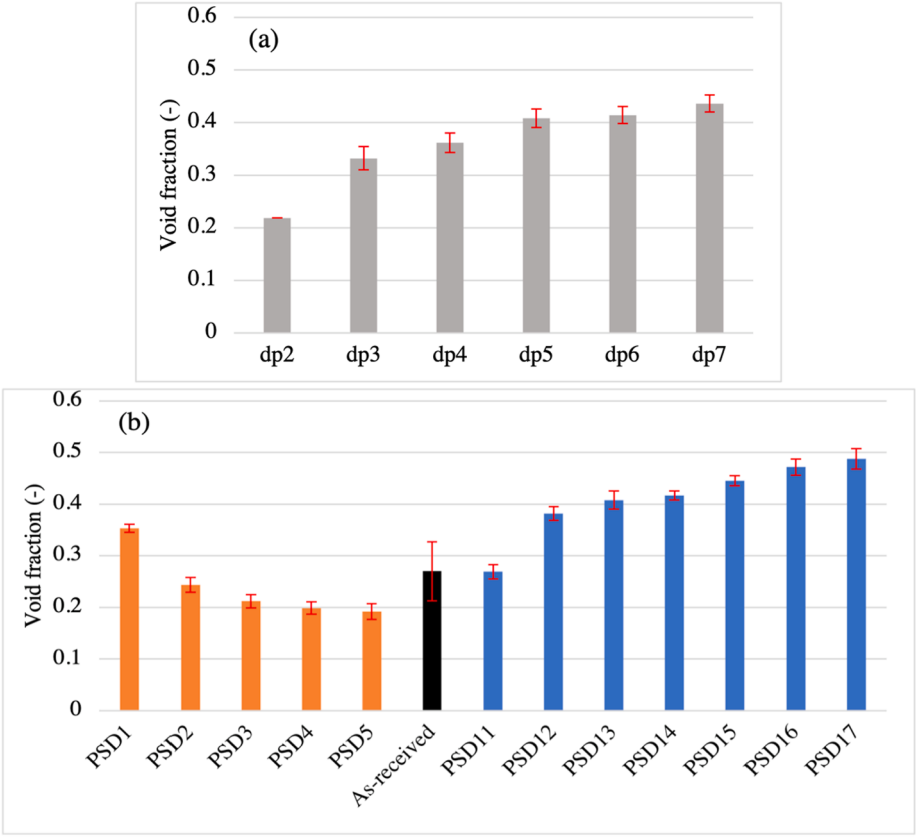

Fig. 2. The void fractions of the monodispersed (a) and the polydispersed samples (b).

of bulk and envelope density.

Prior to proximate and ultimate analyses, a representative sample of biomass char was ground to a particle size below 75 μm. Proximate analysis of the biomass char was measured based on thermogravimetric analysis using TGA8000, PerkinElmer. Volatile matter content was measured by firstly heating around 2 mg of the sample under 50 mL min^{-1} of N_2 from the temperature of 30 °C to 105 °C with the applied heating rate of 100 °C min^{-1}. The sample was held for 10 min to remove moisture in the sample. Then, the temperature was increased to 900 °C at the applied heating rate of 25 °C min^{-1} and held at this temperature for 10 min. Hence, volatile matter content accounted for the mass lost after the drying step according to [31], and it was calculated by

$$\%VM = \frac{m_{dry} - m_{final}}{m_{dry}} \times 100\% \quad (6)$$

Ash content was measured by firstly heating around 2 mg of the sample under 50 mL min^{-1} of N_2 from 30 °C to 105 °C with the applied heating rate of 5 °C min^{-1}. The sample was held for 5 min to remove moisture in the sample. Then, the gas composition was switched to 20% (vol.) of O_2 in N_2, and the temperature was increased to 550 °C and held for 30 min or until the mass became stable. The ash content was accounted for the final mass in comparison to the dried mass according to DIN 51719, which was calculated by

$$\%Ash = \frac{m_{final}}{m_{dry}} \times 100\% \quad (7)$$

Fixed carbon of the sample on dried basis was calculated by the difference, that is, 100 - %VM - %Ash. Ultimate analysis of the biomass char was carried out with EA3000, CHNS-O elemental analyzer from Eurovecto Srl., according to DIN 51732. Higher heating value (HHV) was measured by using a bomb calorimeter, IKA C200. All analysis was repeated three times. Physical properties, proximate analysis, ultimate analysis, and HHV of the sample are provided in Table 4.

Table 4
Physical and chemical properties of the biomass char sample.

Properties	Unit	Average value	Standard deviation
Bulk density	kg m^{-3}	572	45
Envelope density	kg m^{-3}	783	90
Skeleton density	kg m^{-3}	1900	8
Bed void fraction	–	0.27	–
Particle porosity	–	0.59	–
Proximate analysis			
Volatile matter content	%, mass*	8.7	0.1
Ash content	%, mass*	12.3	0.5
Fixed carbon content	%, mass*	77.8	0.7
Ultimate analysis			
C	%, mass*	82.4	0.8
H	%, mass*	0.5	0.0
N	%, mass*	0.5	0.2
O	%, mass*	5.8	0.2
HHV	kJ g^{-1}	27.6	0.1

*Dry basis.

2.3. Measurement of gasification rates

2.3.1. Intrinsic reaction kinetics

Intrinsic kinetic parameters of biomass char gasification with CO_2 were determined using TGA8000 coupled with gas mixing device GMD8000 from PerkinElmer Inc. Biomass char with particle size below 75 μm was used to minimize the effect of intraparticle diffusion. Around 0.5–1.2 mg of the sample was loaded and spread at the bottom of an alumina crucible (diameter of 7 mm and height of 2 mm) as a thin layer to minimize the effect of interparticle diffusion. Reaction gas was fed in the vertical direction down to the crucible, and the total flow rate was kept constant at 50 mL min^{-1} in the standard state (25 °C and 10^5 Pa). The sample was heated from 30 °C to target temperatures, i.e., 770, 800,

830, and 850 °C, at the applied heating rate of 10 °C min^{-1} under N_2 (purity ≥99.996%). Once the target temperature was reached, the gas composition was switched to target concentrations, i.e., 10, 20, 30, and 40% (vol.) of CO_2 (purity ≥99.99%) in N_2. The sample was held at the isothermal condition until there was no mass change. The experimental matrix is provided in the supplementary material, Table S2. Measurement has been carried out with two repetitions for all the conditions, and the repeatability of these measurements is displayed in the supplementarys, Figure S2.

After eliminating the heating part from the TG curves, the results contain mass losses due to both devolatilization and gasification. Therefore, additional experiments were carried out under pure N_2 at the same temperature programs. The devolatilization rates were evaluated from the experimental data by using the first-order reaction equation. The detailed evaluation and the devolatilization curves are provided in the supplementary material, Figure S3. The devolatilization rates were eliminated from the overall results, and only gasification data is acquired by

$$r_{gasification} = r_{overall} - r_{devolatilization} \tag{8}$$

where r is reaction rate in mass basis (g s^{-1}). An example of the TG results after removing devolatilization is shown in Figure S4 in the supplementary material. Then, the conversion of biomass char (X) during gasification was calculated by

$$X = \frac{m_0 - m}{m_0 - m_{ash}} \tag{9}$$

where m_0 is the initial mass at the beginning of gasification, m_{ash} is the weight of ash obtained from the final mass of the experiment, and m is the weight monitored at a given time during gasification.

The conversion rate of biomass char gasification can be described as:

$$\frac{dX}{dt} = k(T, p_{CO2}) \bullet \mathrm{f(X)} \tag{10}$$

where k is the rate constant, which includes the influences of temperature, T, and partial pressure of CO_2, p_{CO2}. The term $f(X)$ is a structural function that represented the changes of active site density with the gasification progress. In this work, the random pore model was applied to estimate the structural function, which yields the overall gasification rate as [32,33]

$$\frac{dX}{dt} = k(T, p_{CO2}) \bullet (1 - \mathrm{X}) \sqrt{1 - \psi} \bullet \ln(1 - \mathrm{X}) \tag{11}$$

After integration of Equation (11) between 0 and X , the equation becomes

$$\left(\frac{2}{\psi}\right) \bullet \left[\sqrt{1 - \psi} \bullet \ln(1 - \mathrm{X}) - 1\right] = \mathrm{k} \bullet \mathrm{t} \tag{12}$$

Figure S5 in the supplementary material shows that the experimental data between X from 0 to 0.8 gave the minimum error to the fitting. Therefore, the structure parameter, ψ, was estimated by using the following expression, where X_f is 0.8:

$$\frac{\left[\sqrt{1 - \psi} \bullet ln(1 - X) - 1\right]}{\left[\sqrt{1 - \psi} \bullet ln\left(1 - X_f\right) - 1\right]} = \frac{t}{t_f} \tag{13}$$

After obtaining the ψ values for each experimental temperature, the intrinsic rate constant, $k_{intrinsic}$, can be determined from Equation (12). Figure S6 in the supplementary material depicts the dependency of ψ on experimental conditions, which followed the definition of the structure parameter, Equation (S5). The fitting performance of RPM to intrinsic reaction rates is provided in Figure S7. It is worth mentioning that the peaks of reaction rate appeared at conversions lower than 0.4, implying the minor effect of inorganic catalysts, as discussed in the literature [34,35].

Kinetic parameters were determined from the nth-order reaction model with the Arrhenius-type of the equation, which has been successfully implemented previously [36]. In order to avoid significant error in the extrapolation of the pre-exponential factor, the equation was normalized by the rate constant of a reference condition as:

$$k_{intrinsic} = k_0 \bullet \exp\left(-\frac{\mathrm{E}}{\mathrm{R}}\left(\frac{1}{\mathrm{T}} - \frac{1}{\mathrm{T_0}}\right)\right) \bullet \left(\frac{\mathrm{P_{CO2}}}{\mathrm{P_{CO2,0}}}\right)^{\mathrm{n}} \tag{14}$$

where, k_0 is the rate constant at the reference condition, E is the activation energy, n is the reaction order, and R is the ideal gas constant. The term T_0 is reference temperature (800 °C), and $P_{CO2,0}$ is reference partial pressure (0.02 MPa). Finally, the estimated kinetic parameters were adjusted to minimize the error between experiments and models (see the supplementary material, Equation (S6) and Figure S8).

2.3.2. The influence of intraparticle diffusion

The same equipment, i.e., TGA8000, was used to measure the apparent reaction rate with the influence of intraparticle diffusion. The monodispersed particle samples were used to observe the effect of intraparticle diffusion. The sample was loaded and spread at the bottom of an alumina crucible as a thin layer to minimize interparticle diffusion. The sample was heated from 30 to 850 °C at the applied heating rate of 10 °C min^{-1} under N_2 flow rate of 50 mL min^{-1}. After the temperature was reached to 850 °C, the gas composition was switched to 40% (vol.) of CO_2 in N_2 at the same total flowrate. The sample was held at the isothermal condition for 3 h. The experiment was repeated 3 times for each particle size.

The heating part was eliminated from the thermogravimetric curve, and overall conversion is determined by Equation (9). The subtraction of devolatilization rate was much simpler than intrinsic reactivity measurement (section 2.3.1) due to distinctive changes in reaction rate. Figure S9 in the supplementary material shows the conversion rate as a function of conversion. The high conversion rate observed at the initial stage of conversion represents devolatilization. Therefore, gasification data was obtained after eliminating this devolatilization part. By applying Equation (11), the rate constant ($k_{particle}$) of char gasification in intraparticle diffusion limitation was determined from the experimental result up to 40% of conversion. The ψ value determined at 850 °C in the previous section was used to calculate the rate constant in this section.

In order to indicate the relative significance of intraparticle diffusion in the apparent rates, the intraparticle effectiveness factor, $\eta_{intraparticle}$, was defined by the following equation.

$$\eta_{intraparticle} = \frac{k_{particle}}{k_{intrinsic}} \tag{15}$$

Thiele modulus, ϕ, can be determined by its correlation with the effectiveness factor. The following equations are the correlation between the effectiveness factor and Thiele modulus for different particle shapes [37,38]

$$\eta_{intraparticle} = \begin{cases} f_c \dfrac{1}{\phi}\left[\dfrac{1}{tanh(3\phi)} - \dfrac{1}{3\phi}\right], sphere \\ f_c \dfrac{1}{\phi}\dfrac{I_1(2\phi)}{I_0(2\phi)}, cylinder \\ f_c \dfrac{tanh(\phi)}{\phi}, plate \end{cases} \tag{16}$$

where, f_c is a correction function expressed as $f_c = \left(1 + \frac{\sqrt{1/2}}{2\phi^2 + 1/(2\phi^2)}\right)^{0.5(1-n)^2}$, and I_0 and I_1 are Bessel function of the first kind. According to microscopic images, Figure S1, the char sample contains mixed particle shapes, especially when particle size is small. However, the aspect ratios of the particles should be higher than 3 to consider the sample as cylinder and plate shapes. Therefore, the

spherical shape model is selected for the main calculation of the intraparticle effectiveness factor in this study. According to the definition of Thiele modulus defined by K.B. Bischoff [39], the expression of Thiele modulus is modified to gasification reaction as

$$\phi = d_p \bullet \sqrt{\frac{n+1}{2 \bullet D_{eff}}} \bullet \frac{k_{intrinsic}}{P^n_{CO_2}} \bullet \frac{\rho_C}{Mw_C} \bullet RT \quad (17)$$

where, d_p is particle diameter, ρ_C is carbon density, and Mw_C is the molecular weight of carbon. Effective diffusivity, D_{eff}, can be determined by least-square minimization using the experimental results of ϕ at the different particle sizes. For the evaluation of bed-scale experiments in the next section, the model, Equation (16) and (17), was applied to estimate the intraparticle effectiveness factor for different particle sizes.

2.3.3. The influence of interparticle diffusion in a packed bed

The apparent rate of char gasification in a packed bed was measured in a macro-thermogravimetric (macro-TG) reactor. The reactor is an externally heated stainless-steel cylinder (grade 253 MA). The internal diameter of the reactor and the length of the heating zone are 40.5 mm and 360 mm, respectively. The reactor temperature was measured by a type N thermocouple placed at the center of the reactor and 20 mm below the sample. The carrier gas flows through the reactor from the bottom to the top of the reactor with product gas generated during the experiment. A ceramic crucible with 20 mm in diameter and 40 mm in height was used to hold the sample. The crucible was connected to a precision balance and hung from the top of the reactor chamber. Fig. 3 displays the schematic drawing of the macro-TG reactor.

Prior to the experiment, the macro-TG reactor was pre-heated to 950 °C, which is the maximum temperature of the reactor. The composition of the carrier gas was 40% (vol.) of CO_2 in N_2 with the total flow rate of 5 L min^{-1} at the standard state. This gas condition was selected to mimic industrial process conditions. The biomass char sample was filled into the ceramic crucible by keeping constant bed volume at 6500 mm^3 (18 mm of the bed height) to maintain constant external diffusion. The crucible was lowered manually to the reactor. The sample was held in the reactor for 3 h. Mass and temperature during the experiment were continuously recorded every 2 s.

Mass loss originated by devolatilization was subtracted from the data according to the same method used in the previous section. Conversion and apparent rate constants (k_{bed}) were determined by using Equation (9) and (11), respectively. In this section, the overall effectiveness factor, $\eta_{overall}$, was defined to indicate the overall effects of diffusion including intraparticle and interparticle scales.

$$\eta_{overall} = \frac{k_{bed}}{k_{intrinsic}} \quad (18)$$

By assuming no interaction between interparticle and intraparticle diffusions, the overall effectiveness factor can be expressed as the product of intraparticle and bed effectiveness factors. Therefore, the bed effectiveness factor,η_{bed}, can be determined by

$$\eta_{bed} = \frac{k_{bed}}{k_{particle}} = \frac{\eta_{overall}}{\int \eta_{intraparticle} \bullet f_o(d_p) dd_p} \quad (19)$$

where $f_o(d_p)$ is the frequency function on a mass basis, which obtained from the particle size distribution measurement. The bed effectiveness factor indicates the contribution of interparticle diffusion to the overall effectiveness factor.

3. Results and discussion

3.1. Intrinsic kinetic parameters

The intrinsic rate constant of char sample measured in this study can be expressed as

$$k_{intrinsic} = \left(2.88 \times 10^{-5} s^{-1}\right) \bullet e^{\left(-\frac{296\ kJ\ mol^{-1}}{R}\left(\frac{1}{T}-\frac{1}{1073\ K}\right)\right)} \cdot \left(\frac{P_{CO2}}{0.02\ MPa}\right)^{0.458} \quad (20)$$

The activation energy of char gasification obtained in this work, i.e., E = 296 kJ mol^{-1}, is slightly higher than those reported in the literature, such as Klose and Wölki [40] (beech wood char, E = 200 kJ mol^{-1}), Haustein et al. [41] (wood-based char, E = 205.4 kJ mol^{-1}), Struis et al. [42] (Firwood char, E = 212 kJ mol^{-1}), Wang et al. [43] (pine char, E = 239 kJ mol^{-1}), Yuan et al. [44] (pine char, E = 248.5 kJ mol^{-1}), and Kramb et al. [45] (pine char, E = 280 kJ mol^{-1}). The reaction order obtained in this work, i.e., n = 0.458, is in the range of the values those have been reported in the literature [36,40,41,46,47], i.e., between 0.369 and 0.7.

Figure 4 shows the Arrhenius plot of the char gasification obtained from this work in comparison to wood-based chars reported in the literature [40–45]. The wide scatter in rate constants among the literature sources illustrates the effects of raw biomass species and pyrolysis conditions on char reactivity. In general, high pyrolysis temperature results in low reactivity chars due to thermal annealing and the loss of catalytic active inorganic elements such as alkali metals [48–50]. The

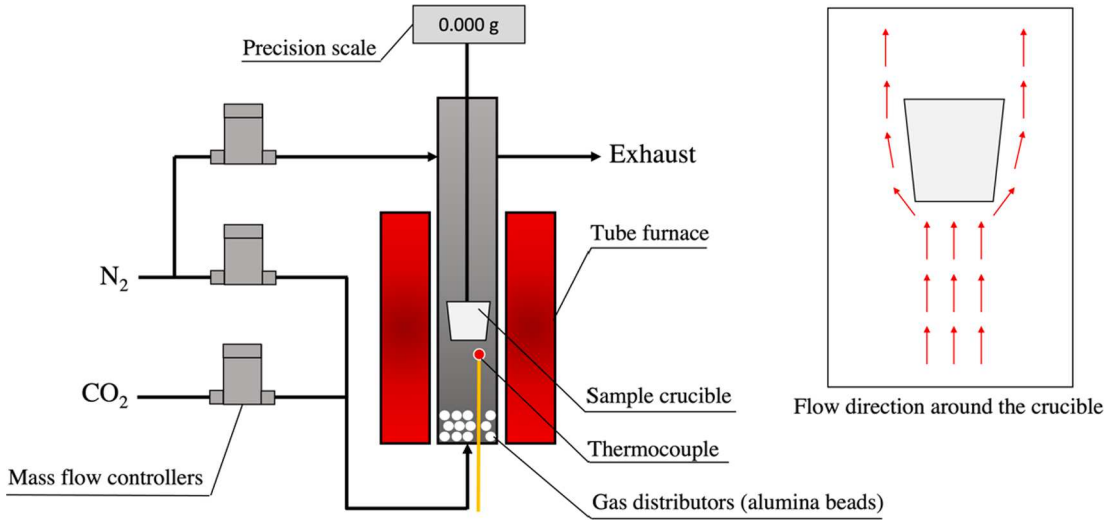

Fig. 3. Measurement of char gasification in a packed bed using a macro-thermogravimetric reactor.

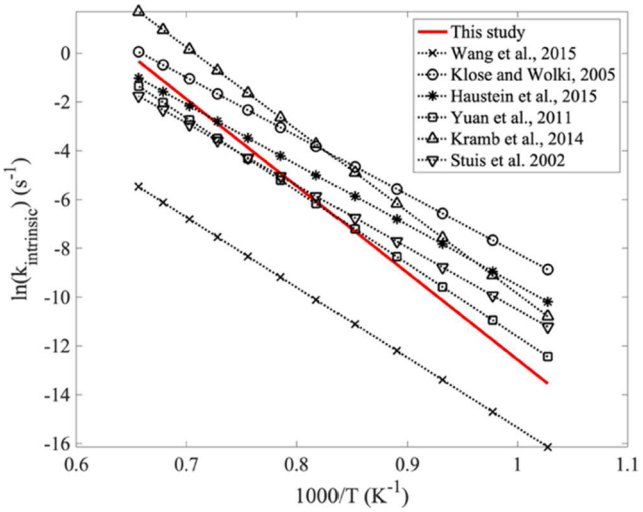

Fig. 4. Arrhenius plots of biomass chars (recalculated from [40–45]).

rate constant of the char in this work stays within the range but lower range among the literature data. Most literature uses biomass char produced at temperatures below 900 °C, which is significantly lower than the char preparation temperature in this study. It should be noted that the kinetic parameters reported from Wang et al. [43] were measured from pine char produced in a fixed bed reactor at temperature of 1100 °C with a long residence time of 90 min, which can explain relatively low reactivity compared to the others.

3.2. Intraparticle diffusion effect at the particle scale

In this section, the apparent reaction rate was measured under the influence of intraparticle diffusion, while the effect of interparticle diffusion was kept minimal. Fig. 5 shows the conversion rates of char gasification with different particle sizes as a function of conversion. The dots represent experimental measurement, while the lines represent the models described by Equation (11). As expected, the conversion rate decreased as the particle size increased due to the effect of intraparticle diffusion. Under the gasification conditions of this study, the apparent reaction rate was nearly identical to the intrinsic reaction rate (Equation (20)), at the particle size of 0.196 mm.

Intraparticle effectiveness factors were determined based on the measured apparent rate constants and the intrinsic rate constant, as shown in Equation (15). Fig. 6 displays the effectiveness factors as a function of the mid-range particle size. The error bars in the vertical direction represent the standard deviations of effectiveness factors, while the horizontal error bars represent the upper and lower sieve sizes.

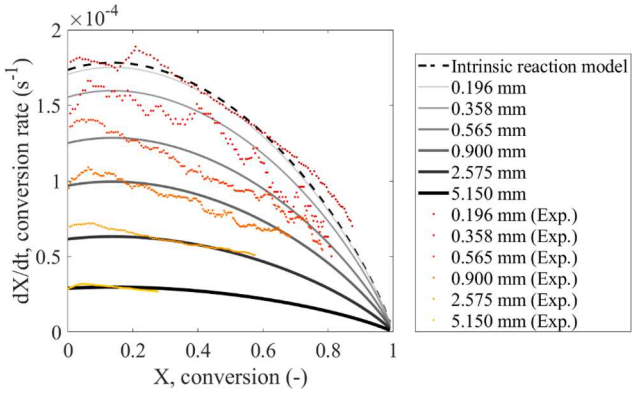

Fig. 5. Conversion rate as a function of conversion. Reaction condition: 850 °C 40% (vol.) CO_2.

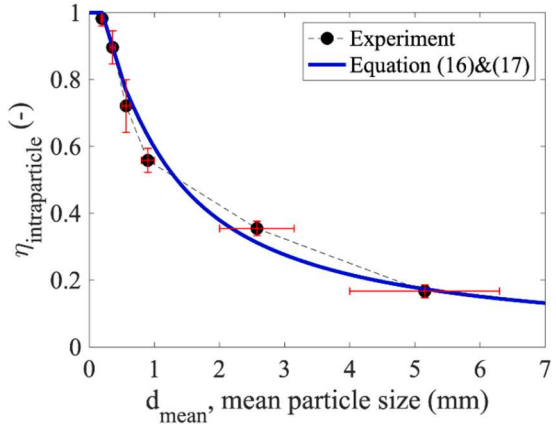

Fig. 6. Intraparticle effectiveness factor as a function of mid-range particle size. Reaction condition: 850 °C 40% (vol.) CO_2.

The effectiveness factor decreased from 0.983 to 0.167 when the particle size increased from 0.196 mm to 5.15 mm. As shown in line plots, the effectiveness factor for sphere particles based on Thiele modulus (Equation (16) and (17)) showed good agreements with the experimental observations.

Fig. 7 shows the plot between Thiele modulus and mid-range particle size. According to the definition of Thiele modulus defined by Bischoff [39], Equation (17), effective diffusivity, D_{eff}, can be determined from the linear fitting in the figure. The effective diffusivity obtained in this work is 1.93×10^{-6} m^2 s^{-1}. It should be noted that the deviation in the particle size due to the sieve sizes may give a small error to the value of effective diffusivity.

Effective diffusivity inside the char particles is affected by both molecular diffusion (D_{AB}) and Knudsen diffusion (D_{KA}) with the relationship of

$$\frac{\varepsilon/\tau}{D_{eff}} = \frac{1}{D_{AB}} + \frac{1}{D_{KA}} \tag{21}$$

where ε and τ are particle porosity and tortuosity, respectively. Tortuosity is an important parameter that determines the diffusivity of CO_2 in particles, but it is a difficult parameter to measure directly in char particles. Meanwhile, the same biomass char should give the same tortuosity regardless of particle size. Therefore, particle tortuosity was assumed to follow the Bruggeman correlation [51] for spherical particles, i.e., $\tau = \varepsilon^{-0.5}$, which gave the value of 1.3. The molecular diffusivity of CO_2 through N_2 was calculated by the model provided by Hirschfelder et al. [52], which gave the value of 2.21×10^{-4} m^2 s^{-1} at

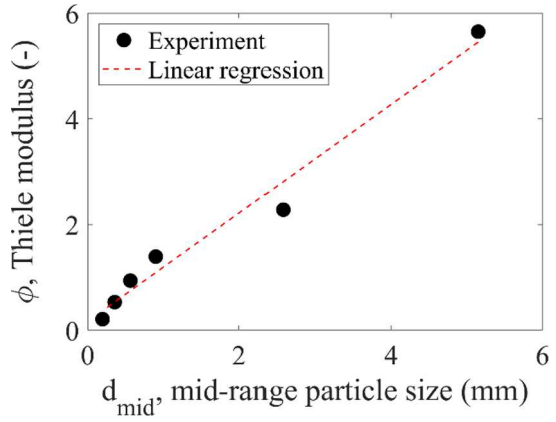

Fig. 7. Thiele modulus as a function of mid-range particle size. Reaction condition: 850 °C 40% (vol.) CO_2.

850 °C. With the estimated values of molecular and effective diffusivities, Knudsen diffusivity can be determined using Equation (21). Furthermore, average pore diameter, d_{pore}, can be estimated from the Knudsen diffusivity equation, which is written as

$$D_{KA} = \frac{d_{pore}}{3}\sqrt{\frac{8\kappa NT}{\pi M_A}} \quad (22)$$

where κ is the Boltzmann constant (1.38×10^{-16} ergs K^{-1}), N is Avogadro constant (6.022×10^{23} molecules mol^{-1}), and M_A is the molecular weight of CO_2. The average pore diameter of biomass char estimated in this work was 17.8 nm, which agree with the typical pore size range of biomass chars reported in the literature [53]. This pore size is in the mesopore range, i.e., 2–50 nm, which has been reported as the major reactive pore surface in gasification reaction [54]. Knudsen number was estimated to be 12.1, which indicate that both molecular and Knudsen diffusions play roles in the effective diffusivity. It means that particle size, pore size, particle porosity, and tortuosity were all important physical parameters that influence intraparticle effectiveness factors. Table S3 in the supplementary material provides the sensitivity of the results against particle shape. The results showed very small differences among different particle shapes. The calculated pore diameters for cylindrical and plate shapes were 17.7 and 17.1 nm, respectively.

3.3. Intraparticle and interparticle diffusion effects in a packed bed

This section discusses the results of the apparent reaction rates measurement in packed beds of biomass char. First, the reaction rates were measured in packed beds consisting of monodispersed particles to represent the effect of particle size without wide distribution. The ratio of the apparent rate measured in this section to the intrinsic rate is defined as overall effectiveness factor according to Equation (18). Intraparticle effectiveness factors for monodispersed particles were calculated from Thiele modulus, i.e., Equation (16) and (17), using average pore diameter determined from the previous section. Hence, bed effectiveness factors can be calculated from Equation (19). Fig. 8 depicts the overall, intraparticle, and bed effectiveness factors of the packed bed as a function of mid-range particle size.

Contrary to the intraparticle effectiveness factor, bed effectiveness factors increased with the increase of particle size. The overall effectiveness factor increased from 0.022 to 0.027 when the particle size increased from 0.196 to 0.9 mm, showing the dominant effects of interparticle diffusion over intraparticle diffusion. At larger particle sizes, the overall effectiveness factor remained almost constant due to the balance between intraparticle diffusion and interparticle diffusion. This can be observed at the particle size larger than 0.9 mm. However, one should note that the plateau in the overall effectiveness factor may not appear for the packed bed with different diffusion lengths due to different interparticle diffusion resistances.

Fig. 9 shows the bed effectiveness factor as a function of void fraction. The bed effectiveness factor increased with the increase of void fraction. As the void fraction increased from 0.22 to 0.41, the bed effectiveness factor increased from 0.031 to 0.11 (increased by factor 3). At the void fraction higher than 0.41 (d_{mid} greater than 0.9 mm), the bed effectiveness factor sharply increased from 0.11 to 0.57 at the void fraction of 0.44 (increased by factor 67). This result suggests that the packed beds with particle sizes larger than 0.9 mm have relatively large bed channels and lower bed tortuosity, resulting in high apparent reaction rate. However, the results require careful interpretation for the two largest particles. The wall effects are commonly observed to affect overall porosity and flow inside packed beds when the bed diameter is below 10 times particle diameters [55,56]. In the diffusion-dominated system, such as in this study, the wall effects change the effective mass diffusivity due to high void fraction and low tortuosity. The two largest particles fall within this range ($D_{bed}/d_{p6} = 7.8$ and $D_{bed}/d_{p7} = 3.9$). However, overall bulk density was not significantly altered by the crucible size within this range (Figure S10 in the supplementary material). Nevertheless, there is still a possibility that the locally high porosity near the wall [55] contributed to the increase in diffusivity and effectiveness factor.

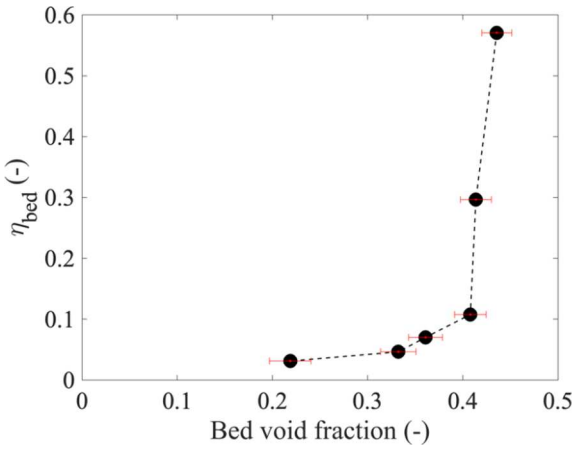

Fig. 9. Bed effectiveness factor as a function of bed void fraction. Reaction condition: 950 °C 40% (vol.) CO_2.

For monodispersed particles, large particles react slower than small particles at the particle scale. However, the effect was reversed at the bed scale because small particles have lower interparticle diffusivity of reactant through bed channels than large particles. Hence, the reactivity may be reduced further if the bed contains both small and large particles, for example, particles with bimodal size distribution or wide size distribution. Fig. 10 shows the comparison of overall effectiveness factors for monodispersed and bimodal particles. With the bimodal particle of 0.8–1 mm and 4–6.3 mm, the overall effectiveness factor showed 11%

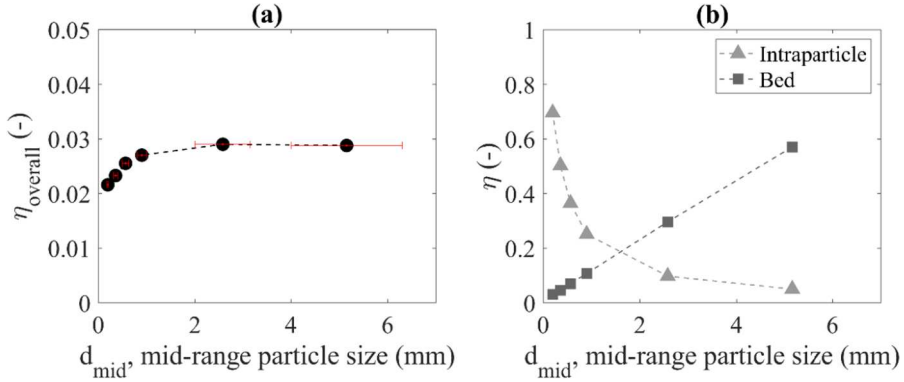

Fig. 8. Overall (a), intraparticle and bed (b) effectiveness factors as a function of mid-range particle size. Reaction condition: 950 °C 40% (vol.) CO_2.

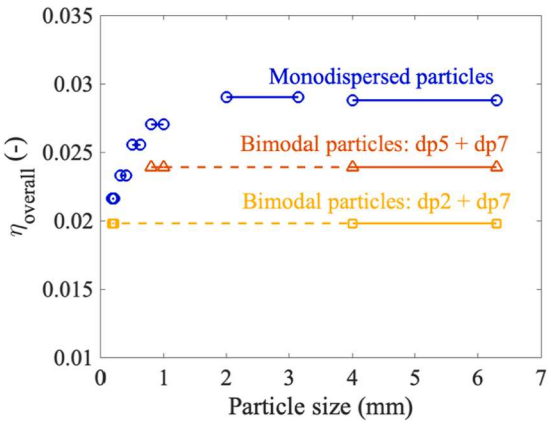

Fig. 10. Overall effectiveness factors in the comparison between monodispersed and bimodal packed beds. Reaction condition: 950 °C 40% (vol.) CO_2.

lower than that of monodispersed particles of 0.8–1 mm. This result verifies the hypothesis that apparent gasification rate of biomass char decreases by the combination of intraparticle and interparticle diffusion limitations in bimodal packed beds. Particles in larger size class contribute to this with low intraparticle effectiveness factors. Meanwhile, particles in smaller size class can fill the bed channels between large particles, resulting in lower bed void fraction and higher bed tortuosity than the bed solely consisting of large particles.

However, the voids between particles that are slightly smaller than particles in smaller size class cannot be filled, and the bed void fraction would not be as low as the bed of solely small particles. Therefore, the diffusivity through the bed of bimodal particles, and thus the bed effectiveness factor, is likely to be the value between the beds of small and large size fractions. Fig. 11 shows the comparison of bed effectiveness factors estimated by Equation (19). The figure depicts the bed effectiveness factors of bimodal particle mixes and monodispersed particles with the smallest and the largest sizes of the mixes. In both bimodal particle mixes, the bed effectiveness factor showed the value between those of small and large particles size classes. However, it is worth mentioning that this value was much closer to that of the small size class than the large size class. These results show the potential to reduce apparent gasification rates by changing particle size distribution in the packed bed.

3.4. Effect of the different PSD on the reaction rate in a packed bed

The previous section demonstrated that the packed beds of biomass char with bimodal particle sizes had lower reaction rates than those of monodispersed particle sizes. However, it is uncommon to yield bimodal particle sizes in industrial size reduction processes, whereas it is possible to change the homogeneity of particle size distributions. Therefore, this section explores the effect of different PSD on the reaction rate in a packed bed.

Fig. 12 shows the overall effectiveness factor as a function of median particle size, i.e., d_{50}, in the packed bed. In the first case, named as "PSD_{small}", the maximum size class in PSD was varied while the minimum size was kept constant at 0.18 mm, i.e., PSD1-5 in Fig. 1. The result of overall effectiveness factors did not give a significant change when d_{50} increased. This occurred due to the beds contain mostly small particles, which will be discussed in detail later. In the second case, named as "PSD_{large}", the minimum size class in PSD was varied while the maximum size was kept constant at 6.3 mm, i.e., PSD11-17. In this case, the overall effectiveness factor firstly increased with d_{50} showing the dominant effects of interparticle diffusion over intraparticle diffusion. Then, the overall effectiveness factor slightly decreased at large d_{50} due to the higher effect of intraparticle diffusion. The maximum overall effectiveness factor is observed at d_{50} of 2.77 mm.

Fig. 13 depicted intraparticle effectiveness factor as a function of d_{50} in the comparison between the bed with monodispersed and polydispersed samples. Intraparticle effectiveness factors in this section were calculated based on the distribution of particle sizes. The intraparticle effectiveness factor of the beds with PSD_{small} have high intraparticle effectiveness factors due to the small size class. Meanwhile, the beds with PSD_{large} have low intraparticle effectiveness factors due to the large size class. The intraparticle effectiveness factor of PSD well followed those of monodispersed particles, ascribed by the Thiele modulus. However, at d_{50} of 0.7 to 0.85 mm, where both PSD_{small} and PSD_{large} samples contain the widest size ranges, the intraparticle effectiveness factors of PSD samples were higher than those of the monodispersed samples. This result was obtained because these PSDs covers small particles down to <0.18 mm, while the monodispersed sample has the minimum particle size of 0.8 mm.

In the packed bed of monodispersed particles, the bed effectiveness factor increased linearly with the mid-range particle size due to uniform bed channel size. However, this is not the case for the bed with polydispersed particles with wide PSD because the wide range of particle size yields non-uniform bed channel sizes. In addition, the channel size is affected by the bimodal size effects, that is, small particles filled large particle's channels. Fig. 14 shows bed effectiveness factor plotted with different screen sizes, i.e., d_{10}, d_{30}, d_{50}, and d_{60}. Bed effectiveness factors were calculated by Equation (19). As observed from Fig. 14(c), the bed effectiveness factor of the bed with PSD does not increase linearly with the median size, d_{50}. At d_{50} <ca. 2.5 mm (d_{min} = 0.9 mm), the bed effectiveness factors of polydispersed samples are lower than those of monodispersed samples at the same median sizes. This result implies that the median particle size does not accurately describe the bed effectiveness factor for the sample with wide PSD. It also emphasizes that particles smaller than 0.9 mm dominated interparticle diffusion due to its function to fill the channels between large particles. This is

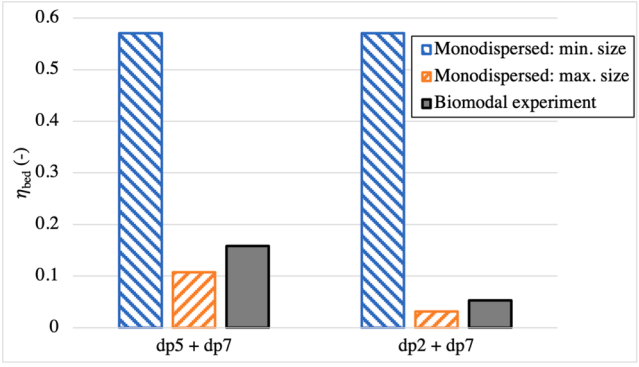

Fig. 11. Bed effectiveness factor in the comparison between monodispersed and bimodal packed beds. Reaction condition: 950 °C 40% (vol.) CO_2.

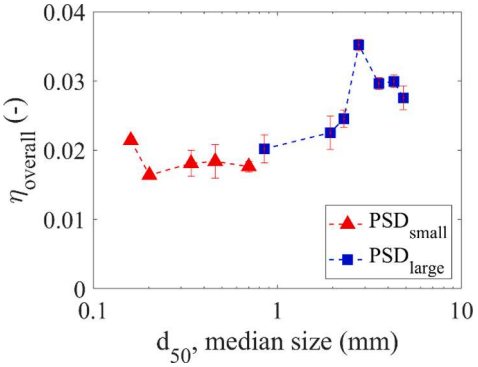

Fig. 12. Overall effectiveness factor as a function of median size. Reaction condition: 950 °C 40% (vol.) CO_2.

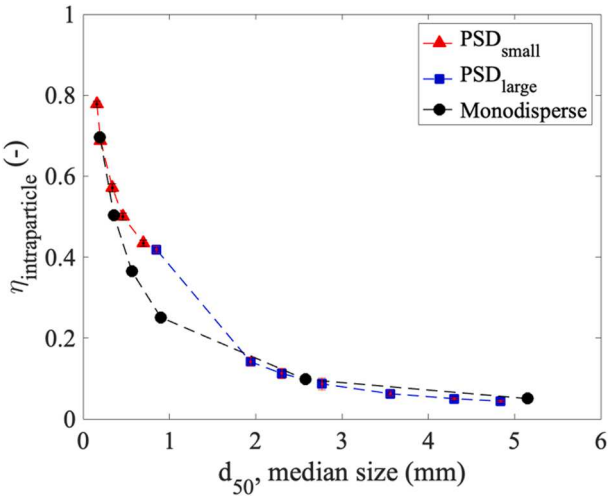

Fig. 13. Intraparticle effectiveness factor as a function of median size. Reaction condition: 950 °C 40% (vol.) CO_2.

confirmed when plotting the bed effectiveness factor with d_{60}, Fig. 14 (d), where a more distinct difference between polydispersed and monodispersed samples is observed. On the other hand, smaller size fractions, i.e., d_{10}, overpredicted the bed effectiveness factor of the beds with wide PSD, as shown in Fig. 14(a). The best agreement of the bed effectiveness factors between polydispersed and monodispersed samples was obtained by plotting it with d_{30} as shown in Fig. 14(b). The bed effectiveness factor of the PSD samples linearly increased when d_{30} increased. Thus, this result shows that the sieve size being passed by 30% of particles can act as an indicator of interparticle diffusion limitation in the bed with wide PSD.

To emphasize the effect of the void fraction on interparticle diffusion, Fig. 15 depicts the bed effectiveness factor as a function of void fraction measured from the bed with PSD_{small} and PSD_{large} in comparison with monodispersed particles. The PSD_{large} follow a similar trend as the monodispersed particles. Meanwhile, the contrary result is obtained in the PSD_{small}, where the bed effectiveness factor decreased with the increase of void fraction. As depicted in Fig. 2, the void fraction of PSD_{small} decreased when the median size increased. This result agrees with the experimental data reported by Zhang et al. [23], who observed the similar trend in PSD of rocks with the median particle size between 0.045 and 3.19 mm. This behavior has been described by the increase in particle aspect ratio when particle size decreased, which is also observed in this study (see Figure S1 in the supplementary material), resulting in higher void fraction in random packing beds of non-spherical particles compared with those of spherical particles [23,57,58]. The literature also showed smaller bed channels when particle size increased [23].

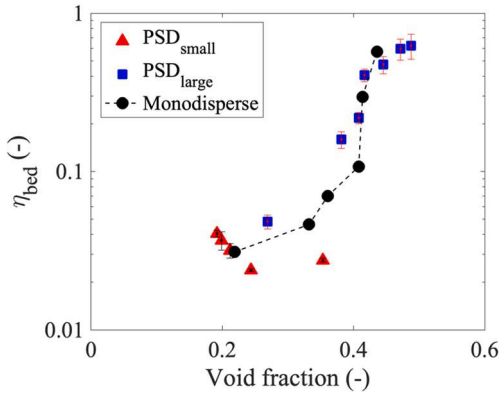

Fig. 15. Bed effectiveness factor as a function of void fraction. Reaction condition: 950 °C 40% (vol.) CO_2.

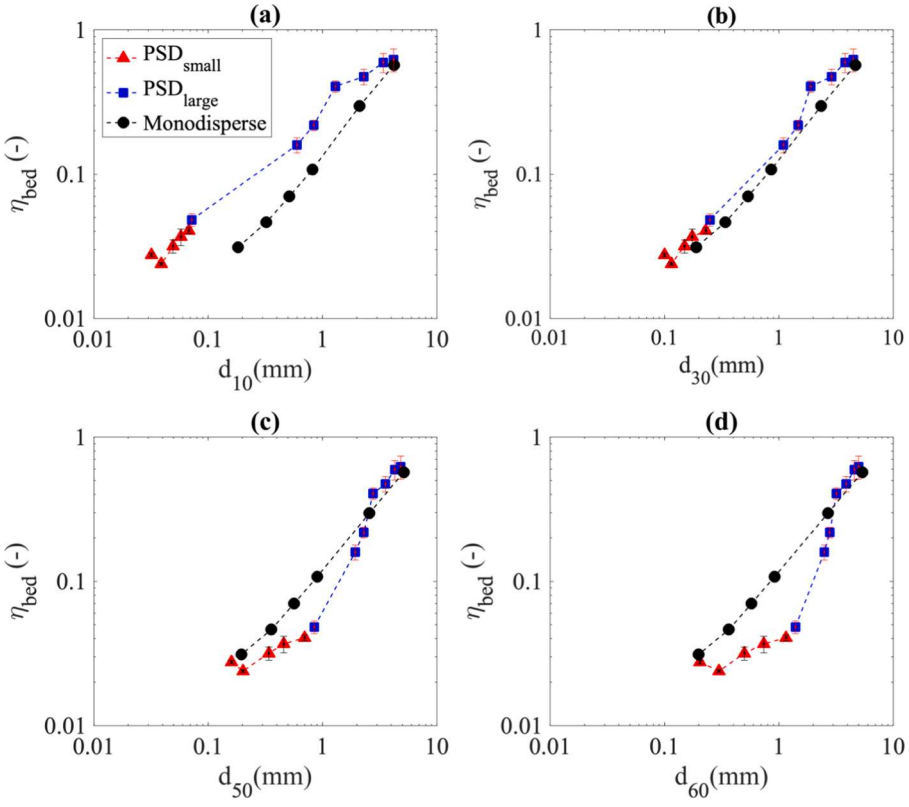

Fig. 14. Bed effectiveness factor as a function of screen sizes being passed 10% (a), 30% (b), 50% (c), and 60% (d) by mass of particles. Reaction condition: 950 °C 40% (vol.) CO_2.

Therefore, it means the bed effectiveness factor of packed beds with very small particles, i.e., d_{50} <0.7 mm, cannot be interpreted by void fraction, but bed channel size and tortuosity must be considered.

Nevertheless, the changes in the overall effectiveness factor of PSD_{small} was not significant, as shown in Fig. 12. In these PSDs, the apparent reaction rate is mainly controlled by interparticle diffusion. However, changing particle size within this small size range (d_{30} = 0.1–0.23 mm) only give small changes in the bed effectiveness factor (from 0.028 to 0.041). Therefore, significant changes in the overall effectiveness factor cannot be observed in the PSD_{small} by the experimental setup used in this study.

4. Conclusions

Under the intraparticle diffusion limitation, larger particles showed lower apparent gasification rates than smaller particles for particle sizes studied in this study (<6.3 mm). Char gasification remained intrinsic reaction rate until the size class of 180–212 μm, but larger particles followed the prediction made by the effectiveness factor using Thiele modulus. Calculated intraparticle diffusivity was 1.93×10^{-6} m^2 s^{-1}, which corresponds to the effective pore diameter of 17.8 nm. This size is within the range of pore size active in the gasification reaction and commonly found in biomass chars.

The effect of interparticle diffusion was first investigated in the packed bed of biomass char using monodispersed particles. The apparent reaction rate increased with the particle size, which contrasts with the results under the intraparticle diffusion control. This is because the beds with large particles have high bed void fraction and low tortuosity, resulted in higher CO_2 diffusivity through channels in the bed. However, the effects of interparticle diffusion and intraparticle diffusion counteract each other, and the overall effects become less pronounced in the bed of particles larger than ca. 1 mm.

A further investigation was carried out on the effect of particle size distribution in packed beds of biomass char using bimodal and polydispersed particles. Independent investigations of two diffusion modes in packed beds showed that intraparticle diffusion effects could be roughly estimated by the median size. On the other hand, interparticle diffusion effects are dominated by smaller particles because of their functions to fill the void between large particles and decrease bed channel size. These two diffusion effects, which are controlled by different fractions in size distributions, interacted and determined the apparent reaction rate of char gasification in packed beds. This observation opens an opportunity to control the overall reaction rate in packed beds by manipulating the particle size distribution.

CRediT authorship contribution statement

Aekjuthon Phounglamcheik: Methodology, Investigation, Formal analysis, Data curation, Writing – original draft. **Markus Bäckebo:** Investigation, Formal analysis. **Ryan Robinson:** Writing – review & editing. **Kentaro Umeki:** Conceptualization, Supervision, Writing – review & editing.

Declaration of Competing Interest

The authors declare that they have no known competing financial interests or personal relationships that could have appeared to influence the work reported in this paper.

Acknowledgements

The authors would like to acknowledge the Swedish Energy Agency for supporting this research (project number: 46974-1) and Cortus Energy AB for providing the biomass char.

Appendix A. Supplementary data

Supplementary data to this article can be found online at https://doi.org/10.1016/j.fuel.2021.122302.

References

[1] Pei M, Petäjäniemi M, Regnell A, Wijk O. Toward a fossil free future with hybrit: Development of iron and steelmaking technology in Sweden and Finland. Metals 2020;10(7):972. https://doi.org/10.3390/met10070972.
[2] Suopajärvi H, Umeki K, Mousa E, Hedayati A, Romar H, Kemppainen A, et al. Use of biomass in integrated steelmaking – Status quo, future needs and comparison to other low-CO2steel production technologies. Appl Energy 2018;213:384–407. https://doi.org/10.1016/j.apenergy.2018.01.060.
[3] Mandova H, Leduc S, Wang C, Wetterlund E, Patrizio P, Gale W, et al. Possibilities for CO 2 emission reduction using biomass in European integrated steel plants. Biomass Bioenergy 2018;115:231–43. https://doi.org/10.1016/j.biombioe.2018.04.021.
[4] Norgate T, Haque N, Somerville M, Jahanshahi S. Biomass as a source of renewable carbon for iron and steelmaking. ISIJ Int 2012;52(8):1472–81. https://doi.org/10.2355/isijinternational.52.1472.
[5] Seo MW, Jeong HM, Lee WJ, Yoon SJ, Ra HW, Kim YK, et al. Carbonization characteristics of biomass/coking coal blends for the application of bio-coke. Chem Eng J 2020;394:124943. https://doi.org/10.1016/j.cej.2020.124943.
[6] Wang C, Mellin P, Lövgren J, Nilsson L, Yang W, Salman H, et al. Biomass as blast furnace injectant - Considering availability, pretreatment and deployment in the Swedish steel industry. Energy Convers Manage 2015;102:217–26. https://doi.org/10.1016/j.enconman.2015.04.013.
[7] Robinson R, Brabie L, Pettersson M, Amovic M, Ljunggren R. An empirical comparative study of renewable biochar and fossil carbon as carburizer in steelmaking. ISIJ Int 2020. https://doi.org/10.2355/isijinternational.isijint-2020-135.
[8] Toloue Farrokh N, Suopajärvi H, Mattila O, Umeki K, Phounglamcheik A, Romar H, et al. Slow pyrolysis of by-product lignin from wood-based ethanol production– A detailed analysis of the produced chars. Energy 2018;164:112–23.
[9] Phounglamcheik A, Wretborn T, Umeki K. Increasing efficiency of charcoal production with bio-oil recycling. Energy Fuels 2018;32(9):9650–8. https://doi.org/10.1021/acs.energyfuels.8b02333.
[10] Kastanaki E, Vamvuka D. A comparative reactivity and kinetic study on the combustion of coal-biomass char blends. Fuel 2006;85(9):1186–93. https://doi.org/10.1016/j.fuel.2005.11.004.
[11] Okumura Y, Hanaoka T, Sakanishi K. Effect of pyrolysis conditions on gasification reactivity of woody biomass-derived char. Proc Combust Inst 2009. https://doi.org/10.1016/j.proci.2008.06.024.
[12] Fermoso J, Gil MV, Pevida C, Pis JJ, Rubiera F. Kinetic models comparison for non-isothermal steam gasification of coal-biomass blend chars. Chem Eng J 2010;161(1-2):276–84. https://doi.org/10.1016/j.cej.2010.04.055.
[13] Zuo H bin, Zhang PC, Zhang JL, Bi XT, Geng WW, Wang GW. Isothermal CO2 gasification reactivity and kinetic models of biomass char/anthracite char. BioResources 2015;10. https://doi.org/10.15376/biores.10.3.5233-5241.
[14] Kajitani S, Suzuki N, Ashizawa M, Hara S. CO2 gasification rate analysis of coal char in entrained flow coal gasifier. Fuel 2006. https://doi.org/10.1016/j.fuel.2005.07.024.
[15] Gómez-Barea A, Ollero P, Fernández-Baco C. Diffusional effects in CO2 gasification experiments with single biomass char particles. 1. Experimental investigation. Energy Fuels 2006;20(5):2202–10. https://doi.org/10.1021/ef050365a.
[16] Guizani C, Escudero Sanz FJ, Salvador S. Influence of temperature and particle size on the single and mixed atmosphere gasification of biomass char with H2O and CO2. Fuel Process Technol 2015;134:175–88. https://doi.org/10.1016/j.fuproc.2015.01.031.
[17] Shen Z, Xu J, Liu H, Liang Q. Modeling study for the effect of particle size on char gasification with CO2. AIChE J 2017;63(2):716–24. https://doi.org/10.1002/aic.v63.210.1002/aic.15417.
[18] Mani T, Mahinpey N, Murugan P. Reaction kinetics and mass transfer studies of biomass char gasification with CO2. Chem Eng Sci 2011;66(1):36–41. https://doi.org/10.1016/j.ces.2010.09.033.
[19] Thiele EW. Relation between catalytic activity and size of particle. Ind Eng Chem 1939;31(7):916–20. https://doi.org/10.1021/ie50355a027.
[20] Schulze S, Nikrityuk P, Abosteif Z, Guhl S, Richter A, Meyer B. Heat and mass transfer within thermogravimetric analyser: From simulation to improved estimation of kinetic data for char gasification. Fuel 2017;187:338–48. https://doi.org/10.1016/j.fuel.2016.09.048.
[21] Zhang Y, Geng P, Zheng Y. Exploration and practice to improve the kinetic analysis of char-CO2 gasification via thermogravimetric analysis. Chem Eng J 2019;359:298–304. https://doi.org/10.1016/j.cej.2018.11.122.
[22] Ollero P, Serrera A, Arjona R, Alcantarilla S. Diffusional effects in TGA gasification experiments for kinetic determination. Fuel 2002. https://doi.org/10.1016/S0016-2361(02)00126-6.
[23] Zhang S, Liu W, Granata G. Effects of grain size gradation on the porosity of packed heap leach beds. Hydrometallurgy 2018;179:238–44. https://doi.org/10.1016/j.hydromet.2018.06.014.
[24] Keyser M, Conradie M, Coertzen M, Vandyk J. Effect of coal particle size distribution on packed bed pressure drop and gas flow distribution. Fuel 2006;85(10-11):1439–45. https://doi.org/10.1016/j.fuel.2005.12.012.

[25] Zhou T, Yang S, Wei Y, Hu J, Wang H. Impact of wide particle size distribution on the gasification performance of biomass in a bubbling fluidized bed gasifier. Renewable Energy 2020;148:534–47. https://doi.org/10.1016/j.renene.2019.10.059.
[26] Luckos A, Bunt JR. Pressure-drop predictions in a fixed-bed coal gasifier. Fuel 2011;90(3):917–21. https://doi.org/10.1016/j.fuel.2010.09.020.
[27] Koekemoer A, Luckos A. Effect of material type and particle size distribution on pressure drop in packed beds of large particles: Extending the Ergun equation. Fuel 2015;158:232–8. https://doi.org/10.1016/j.fuel.2015.05.036.
[28] Cortus AB. Cortus AB, Sweden. Cortus Energy n.d. https://cortus.se (accessed April 16, 2020).
[29] Ithaka Institute. The European Biochar Certificate 2021. https://www.european-biochar.org/en (accessed July 30, 2021).
[30] Certificate TEB. The European Biochar Certificate n.d. https://www.european-biochar.org/en.
[31] Calvelo Pereira R, Kaal J, Camps Arbestain M, Pardo Lorenzo R, Aitkenhead W, Hedley M, et al. Contribution to characterisation of biochar to estimate the labile fraction of carbon. Org Geochem 2011;42(11):1331–42. https://doi.org/10.1016/j.orggeochem.2011.09.002.
[32] Bhatia SK, Perlmutter DD. A random pore model for fluid-solid reactions: I. Isothermal, kinetic control. AIChE J 1980;26(3):379–86. https://doi.org/10.1002/aic.v26:310.1002/aic.690260308.
[33] Lin L, Strand M. Investigation of the intrinsic CO2gasification kinetics of biomass char at medium to high temperatures. Appl Energy 2013;109:220–8. https://doi.org/10.1016/j.apenergy.2013.04.027.
[34] Zhang Y, Ashizawa M, Kajitani S, Miura K. Proposal of a semi-empirical kinetic model to reconcile with gasification reactivity profiles of biomass chars. Fuel 2008;87(4-5):475–81. https://doi.org/10.1016/j.fuel.2007.04.026.
[35] Ding L, Zhang Y, Wang Z, Huang J, Fang Y. Interaction and its induced inhibiting or synergistic effects during co-gasification of coal char and biomass char. Bioresour Technol 2014;173:11–20. https://doi.org/10.1016/j.biortech.2014.09.007.
[36] Kreitzberg T, Haustein HD, Benjamin Gövert RK. Investigation of Gasification Reaction of Pulverized Char Under N2/CO2 Atmosphere in a Small-Scale Fluidized Bed Reactor. J Energy Resour Technol 2016;138:42207–14. https://doi.org/10.1115/1.4032791.
[37] Levenspiel O. Chemical reaction engineering. 1999. https://doi.org/10.1021/ie990488g.
[38] Hong J, Hecker WC, Fletcher TH. Improving the accuracy of predicting effectiveness factors for mth order and Langmuir rate equations in spherical coordinates. Energy Fuels 2000;14(3):663–70. https://doi.org/10.1021/ef9902193.
[39] Bischoff KB. Effectiveness factors for general reaction rate forms. AIChE J 1965;11(2):351–5. https://doi.org/10.1002/(ISSN)1547-590510.1002/aic.v11:210.1002/aic.690110229.
[40] Klose W, Wolki M. On the intrinsic reaction rate of biomass char gasification with carbon dioxide and steam. Fuel 2005;84(7-8):885–92. https://doi.org/10.1016/j.fuel.2004.11.016.
[41] Haustein HD, Kreitzberg T, Gövert B, Massmeyer A, Kneer R. Establishment of kinetic parameters of particle reaction from a well-stirred fluidized bed reactor. Fuel 2015;158:263–9. https://doi.org/10.1016/j.fuel.2015.05.038.
[42] Struis RPWJ, von Scala C, Stucki S, Prins R. Gasification reactivity of charcoal with CO2. Part I: conversion and structural phenomena. Chem Eng Sci 2002;57(17):3581–92. https://doi.org/10.1016/S0009-2509(02)00254-3.
[43] Wang G, Zhang J, Hou X, Shao J, Geng W. Study on CO2 gasification properties and kinetics of biomass chars and anthracite char. Bioresour Technol 2015;177:66–73. https://doi.org/10.1016/j.biortech.2014.11.063.
[44] Yuan S, Chen X-li, Li J, Wang F-chen. CO2 gasification kinetics of biomass char derived from high-temperature rapid pyrolysis. Energy Fuels 2011;25(5):2314–21. https://doi.org/10.1021/ef200051z.
[45] Kramb J, Konttinen J, Gómez-Barea A, Moilanen A, Umeki K. Modeling biomass char gasification kinetics for improving prediction of carbon conversion in a fluidized bed gasifier. Fuel 2014;132:107–15. https://doi.org/10.1016/j.fuel.2014.04.014.
[46] Risnes H, Sørensen LH, Hustad JE. CO2 reactivity of chars from wheat, spruce and coal. Prog Thermochem Biomass Convers 2008. https://doi.org/10.1002/9780470694954.ch4.
[47] Galgano A, Di Blasi C, Horvat A, Sinai Y. Experimental validation of a coupled solid- and gas-phase model for combustion and gasification of wood logs. Energy Fuels 2006;20(5):2223–32. https://doi.org/10.1021/ef060042u.
[48] Phounglamcheik A, Wang L, Romar H, Kienzl N, Broström M, Ramser K, et al. Effects of pyrolysis conditions and feedstocks on the properties and gasification reactivity of charcoal from woodchips. Energy Fuels 2020;34(7):8353–65. https://doi.org/10.1021/acs.energyfuels.0c00592.
[49] Schneider C, Walker S, Phounglamcheik A, Umeki K, Kolb T. Effect of calcium dispersion and graphitization during high-temperature pyrolysis of beech wood char on the gasification rate with CO2. Fuel 2021;283:118826. https://doi.org/10.1016/j.fuel.2020.118826.
[50] Kreitzberg T, Wirch N, Bormann C, Pielsticker S, Hatzfeld O, Mayer J, et al. Thermally induced changes in microstructure and reactivity of biogenic and fossil fuel particles. Appl Energy 2019;254:113607. https://doi.org/10.1016/j.apenergy.2019.113607.
[51] Bruggeman DAG. Berechnung verschiedener physikalischer Konstanten von heterogenen Substanzen. I. Dielektrizitätskonstanten und Leitfähigkeiten der Mischkörper aus isotropen Substanzen. Ann Phys 1935;416(7):636–64. https://doi.org/10.1002/andp.19354160705.
[52] Hirschfelder JO, Bird RB, Spotz EL. The transport properties of gases and gaseous mixtures. II. Chem Rev 1949;44(1):205–31. https://doi.org/10.1021/cr60137a012.
[53] Wedler C, Span R. A pore-structure dependent kinetic adsorption model for consideration in char conversion – Adsorption kinetics of CO2 on biomass chars. Chem Eng Sci 2021;231:116281. https://doi.org/10.1016/j.ces.2020.116281.
[54] Di Blasi C. Combustion and gasification rates of lignocellulosic chars. Prog Energy Combust Sci 2009;35(2):121–40. https://doi.org/10.1016/j.pecs.2008.08.001.
[55] de Klerk A. Voidage variation in packed beds at small column to particle diameter ratio. AIChE J 2003;49(8):2022–9. https://doi.org/10.1002/aic.690490812.
[56] Bale S, Sathe M, Ayeni O, Berrouk AS, Joshi J, Nandakumar K. Spatially resolved mass transfer coefficient for moderate Reynolds number flows in packed beds: Wall effects. Int J Heat Mass Transf 2017;110:406–15. https://doi.org/10.1016/j.ijheatmasstransfer.2017.03.052.
[57] Ouchiyama N, Tanaka T. Porosity estimation for random packings of spherical particles. Ind Eng Chem Fundam 1984;23(4):490–3. https://doi.org/10.1021/i100016a019.
[58] Prior JMV, Almeida I, Loureiro JM. Prediction of the packing porosity of mixtures of spherical and non-spherical particles with a geometric model. Powder Technol 2013;249:482–96. https://doi.org/10.1016/j.powtec.2013.09.006.